

Viscoelastic Parameter Estimation Based on Spectral Analysis

Hani Eskandari, *Student Member, IEEE*, Septimiu E. Salcudean, *Fellow, IEEE*,
and Robert Rohling, *Member, IEEE*

Abstract—This paper introduces a new technique for the robust estimation of relaxation-time distribution in tissue. The main novelty is in the use of the phase of transfer functions calculated from a time series of strain measurements at multiple locations. Computer simulations with simulated measurement noise demonstrate the feasibility of the approach. An experimental apparatus and software were developed to confirm the simulations. The setup can be used both as a rheometer to characterize the overall mechanical properties of a material or as a vibro-elastography imaging device using an ultrasound system. The algorithms were tested on tissue mimicking phantoms specifically developed to exhibit contrast in elasticity and relaxation time. The phantoms were constructed using a combination of gelatin and a polyvinyl alcohol sponge to produce the desired viscoelastic properties. The tissue parameters were estimated and the elasticity and relaxation time of the materials have been used as complementary features to distinguish different materials. The estimation results are consistent with the rheometry, verifying that the relaxation time can be used as a complementary feature to elasticity to delineate the mechanical properties of the phantom.

I. INTRODUCTION

Mechanical properties of soft tissue are known to be affected by malignancies and abnormalities. Stiffness is the mechanical property that has been most widely studied. Previous papers have shown that benign breast lesions are four times as stiff as the background tissue, and carcinomas are eight times stiffer than fibroadenoma [1]. Ultrasound elastography has emerged as a new imaging modality for depicting variations in tissue stiffness, but sensitivity and specificity are still being explored. For example, in a recent paper, 14 patients with breast pathology were studied, six of whom appeared to have benign lesions after biopsy and seven had malignancies [2]. Ultrasound elastography, however, could not discriminate the benign tissue, but it was successful in detecting most of the malignant tumors. Imaging of the mechanical properties in soft tissue to investigate or monitor the pathological changes in the body, generally referred to as elastography, has been widely studied in the past two decades [1]–[12].

Elasticity is known to correlate with the physical structure of soft tissue, however, viscosity can be a means to describe metabolism-dependent features. Carcinomas with

Manuscript received September 19, 2007; accepted January 22, 2008.

The authors are with the Department of Electrical and Computer Engineering, University of British Columbia, Vancouver, BC, Canada (e-mail: times@ece.ubc.ca).

Digital Object Identifier 10.1109/TUFFC.2008.839

high blood vessel concentration exhibit higher viscosity than the surrounding area. In [13], 15 patients with different breast pathologies were examined, and the cancerous breast tissue was seen to be on average 4.4 ± 3.2 times more viscous than the surrounding tissue. Estimation of the tissue viscosity recently has been studied by a number of groups. Chen *et al.* [14] analyzed the dispersion of narrow-band shear waves in homogeneous soft tissue. From the phase of the dissipating wave at different locations, they could estimate the shear wave velocity that, in turn, is related to the shear elasticity and viscosity. Cathe-line *et al.* [15] measured the overall viscoelastic properties by analyzing the speed and attenuation of a transverse wave at several frequencies. Insana *et al.* [16] used ultrasound to image the deformation of soft tissue due to a compressional step force. Using the theory of viscoelastic solids, they modeled the relaxation of the material by two exponentials: one with a low and the other with a high time constant. At frame rates less than 4 frames/second, they were able to detect the dynamic creep and relaxation in the tissue that enabled them to quantify a small time constant of about 1 s and a long time constant of nearly 200 s [17]. Bercoff *et al.* [18] measured the temporal variation of the shear wave inside a homogeneous phantom and compared it with the waveform of a simulated viscoelastic model. The parameters that would yield the most similarity between the simulation and the experimental waveforms were related to the mechanical parameters of the homogeneous phantom. Sinkus *et al.* [19] described a technique to reconstruct the viscosity as well as the anisotropic components of elasticity using magnetic resonance elastography (MRE). Although they obtained a good separation between malignant, benign, and background breast tissue using elasticity, the shear viscosity did not seem to be a significant and discriminating feature. Acoustic remote palpation introduced in [9] has been used by Girnyk *et al.* [20] to create a dynamic strain field and to estimate the dynamic properties of the tissue. They were able to characterize the phantoms and tissue samples *in vitro* at the focal point of vibration, assuming homogeneity in the medium. In order to measure the dynamic properties of the vitreous body in the human eye, Walker *et al.* [21] quantified the step response of the tissue due to a remotely-induced acoustic radiation step force. Work is ongoing to improve sensitivity and specificity of these techniques to make them suitable for routine clinical use.

As an alternative approach, Turgay *et al.* [11] showed a new technique that modeled soft tissue with a series of

Voigt elements and added inertia. The proposed reconstruction technique involved solving an inverse problem for the model parameters such that the error between modeled and measured displacements was minimized. Preliminary simulation results showed promise for the reconstruction of the viscosity as well as elasticity. Also, spectral analysis of the time series of displacements was used to yield a robust elasticity estimation of the medium. The transfer functions calculated between displacements at different locations were used to characterize the viscoelastic properties independent of the model assumption. Salcudean *et al.* [12] used the concept of transfer functions to delineate the prostate boundaries in phantom and experiments *in vivo*.

The transfer function concept will be explored in more detail in the present work. In particular, the phase and the imaginary parts of the transfer functions will be shown to be suitable means for identifying the dynamic properties of the tissue. The relationships between viscoelastic properties and transfer functions will be explored through simulations and phantom experiments and validated using a rheometer and small samples of material. The overall purpose is to study the fundamentals of viscoelastic parameter identification in a controlled environment.

In order to characterize the ability of imaging methods to measure viscoelastic properties of tissue, there is a need for tissue mimicking materials with controllable static and dynamic properties. There is a broad collection of literature on elasticity phantoms using gelatin mixtures [22], [23], agar composites [24], or polyvinyl alcohol (PVA) [25]. Various techniques have been used to induce viscosity contrast in phantoms. It is known that increasing the concentration of gelatin in the gelatin-based phantoms will increase both the elasticity and the viscosity of the material [26]. At low concentrations (i.e., less than 10%) the dependency of the elasticity parameter on the gelatin concentration was seen to be higher than that of the viscosity. Therefore, increasing the proportion of gelatin in water can be used to mimic a hard and viscous lesion with a higher time constant [17], [21]. However, based on the rheology data shown in Section V, at concentrations above 10%, the time constant of the gelatin phantom remains nearly unchanged with respect to the gelatin percentage in water. Therefore, increasing the gelatin concentration results in a stiffer and more viscous phantom, but the relaxation time of the material does not change. Using agents such as glycerol [11], [20], glutaraldehyde [27], or formaldehyde [17], [23] that increase the amount of cross-linking in the gelatin is another way to elevate the viscous effect. In most cases, the cross-linking will affect the elastic and viscous properties as well as the speed of sound in the tissue. In this work, we induce a local inclusion in the phantom by using a material different from the background. It is shown that a PVA sponge can be used as an inclusion in a gelatin-based phantom to control the contrast of the static or dynamic mechanical parameters within the tissue.

As an overview, this paper aims to reconstruct the local viscoelastic parameters of soft tissue. The reconstruction

techniques are verified by simulating a one-dimensional (1-D) network of Voigt elements as a mechanical model of tissue. A transient force is generated and applied to the tissue model, and the displacements at designated locations are measured. Using the acquired displacements, the tissue parameters are identified as explained in the following sections. The ability of the proposed methods to detect elastic and viscous lesions in soft tissue are tested on tissue mimicking materials. The experimental setup is capable of vibrating a small sample with a filtered wide-band excitation, measuring the force and observing the motion ultrasonically over a short period of time. Next, the magnitude and phase of the displacement spectra are analyzed and associated with the viscoelastic properties of the material using well-known parameter identification techniques. From the resulting property calculations, cross-sectional images of viscoelastic properties are generated.

II. MODELS

Soft tissue is known to have nonlinear behavior due to external excitations. Effects such as hysteresis, large deformation, and nonlinear and time-varying mechanical properties can generate higher order harmonics. These nonlinearities are seen to have a rather insignificant effect on the response of most soft tissues at small strains [27]; thus, it is viable to adopt a linear framework in order to analyze and model the response of the soft tissue.

A. Linear Viscoelastic Model

A mechanical structure comprises elastic properties, viscous properties, and inherent density. The elastic behavior of a structure makes it resilient to an external force or deformation. A purely elastic element will vibrate infinitely in response to a momentary excitation. The elasticity in soft tissue can be modeled by a finite number of spring elements in the direction of compression, assuming the compression to be unidirectional. However, due to internal friction and material relaxation effects, a damping term is introduced in the vibration. This effect, which is a liquid-like behavior of soft tissue, is mostly induced by the viscosity of the material. In the theory of viscoelastic solids, viscosity can be modeled by damper elements. Assuming linearity, the force-velocity relationship of the dampers is linear, as well as the force-displacement relationship of the springs. Any element that bears mass exhibits a linear relationship between force and acceleration. Hence, tissue can be modeled as a set of interconnected elements, each being composed of a spring, a damper and a point mass.

Usually, the inertia in the soft tissue can be ignored at low frequencies, considering the relatively low density of human tissue, which is close to that of water. It will be shown in Section V that this approximation is valid in the experiments at frequencies below 50 Hz, depending on the phantom or tissue material. Therefore, at low frequen-

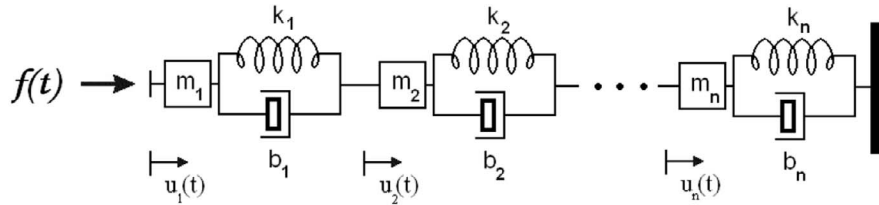


Fig. 1. One-dimensional model of soft tissue with springs, dampers, and masses, assembled as Voigt elements. In the present work, the tissue is considered bound at one end and excited dynamically from the other end. By measuring the displacements with the help of ultrasound, the parameters of the model can be identified.

cies, the tissue can be modeled by a series of springs and dampers. For an incremental region in the tissue, these two components can be either in parallel, which results in the Voigt model, or in series, which gives the Maxwell model. A 1-D model consisting of several Voigt elements with added inertia is shown in Fig. 1. It has been shown that the Voigt model is more accurate in describing the dynamics of the soft tissue [15].

The constitutive relation between the stress (σ) and strain (ϵ) of a Voigt element is a linear first order differential equation as follows:

$$\mu\epsilon(t) + \eta\dot{\epsilon}(t) = \sigma(t), \quad (1)$$

where μ is the Young's modulus or elasticity and η is the viscosity. By ignoring the densities in Fig. 1, the model will contain a series of Voigt elements [28]. The equation of motion for this model can be obtained by discretizing (1). For a typical element i , this gives:

$$k_i[u_i(t) - u_{i+1}(t)] + b_i[\dot{u}_i(t) - \dot{u}_{i+1}(t)] = f(t), \quad (2)$$

where k_i is the stiffness of the i^{th} element and b_i is the viscous damping coefficient. $f(t)$ is the applied force and is the same at every point in the network as the effect of inertia has been ignored. The interested reader can refer to [11] for a detailed analysis of such a model as well as the relationships between the discrete model parameters and the tissue mechanical properties.

When a dynamic compression is applied to a nonhomogeneous sample of finite dimensions, the resulting motion will be determined by several factors. These factors include the method of excitation, the boundary conditions, mode conversion, reflection, refraction, nonlinear response, and other complex phenomena. This investigation attempts to create axial motion and minimize other motions through careful design of the experimental apparatus. As will be shown in Section V, by applying a distributed force on the surface of the phantom, the out-of-plane components of the stress tensor can be minimized, and a state of plane-stress can be approximated. The boundary conditions and the excitation method are carefully controlled. The result is that the axial motion and its spatial variations can be tracked by means of ultrasound, and a tissue model can be used to identify the mechanical parameters in the tissue.

Two key assumptions are made for modeling the tissue response: the axial strain response of tissue to the

axial excitation is linear; and the linear relationship between axial strains at different tissue locations in response to the axial excitation can be described by a first order lead-lag relationship, i.e., an elastic component and a viscous component arranged as a Kelvin-Voigt model [11], [21], [28]–[30]. Such a dynamic system can account for the energy dissipation in the system and justify the observed phase change. The first assumption can be supported by the measurement of the coherence function between the excitation and the estimated displacements. This value, which is seen to be higher than 0.96 in the experiments in Section V, provides a measure of the proportion of the input energy that is transferred into axial tissue motion in a linear fashion [31].

Introducing a comprehensive model that predicts all the nonlinear effects present in the medium is beyond the scope of this paper. In fact, in the aforementioned linear 1-D model, the lateral motions and nonsymmetric deformations are ignored. To justify the use of such a model in experiments, a uniform and symmetric excitation should be applied to the phantom. Also, the boundary conditions should be controlled to minimize the shear effects and induce a low-speed compressional wave in the medium. When these conditions are satisfied and a nearly plane-stress state can be maintained in the medium, the speed of the longitudinal wave from the excitation (in contrast to approximately 1540 m/s for ultrasound) can be as low as $c = \sqrt{E/\rho}$ for finite cross-sectional volumes with free sides [32]. In soft tissues, the Young's modulus (E) is approximately 10 kPa and the density (ρ) is close to 1000 kg/m³, which result in a phase velocity of $c = 3.2$ m/s. These calculations are valid for wavelengths that are large compared to the cross-sectional dimension of the sample [33]. Because pulse-based ultrasound is used to measure the tissue motion, it does not provide an instantaneous snapshot of the displacements at a specific time, but given the relatively small excitation frequency (< 30 Hz), slow excitation phase velocity (3.2 m/s) and relatively fast pulse velocity (1540 m/s), this source of error is negligible. Assuming linearity, a given excitation frequency will produce localized tissue motion at that frequency at all locations within the tissue. So the data acquisition frame-rate of ultrasound is set greater than twice the maximum applied excitation frequency to satisfy the Nyquist requirement. As will be shown in Section V, by applying proper boundary conditions and excitation, the axial motion of the tissue from the excitation can be tracked easily by means of ultra-

sound, and the proposed model can be used to identify the mechanical parameters in the tissue. The experiments are constructed in such a way that the axial motion is the most dominant component in the medium so the model is appropriate. Achieving or circumventing these same conditions in experiments *in vivo* is an acknowledged challenge and is the subject of ongoing study.

B. Spectral Analysis and the Transfer Functions

If the linear network in Fig. 1 is excited by a single frequency force waveform, the displacements and local strains will have the same frequency, but different amplitudes and phase lags. If the force spectrum is wide-band, the spectra of the displacements and strains also will cover a range of frequencies. The shape of each spectrum depends on the model parameters, i.e., the mechanical properties of tissue.

The transfer functions between the applied force and the nodal displacements were studied in previous work [11]. Wherever the force could not be measured, the transfer functions were computed by taking the displacement of one of the blocks as the reference. The low-frequency asymptotes of the transfer functions were correlated with the quasistatic properties of the tissue to delineate the inclusions and the anatomical boundaries [12]. Appendix A includes a review of the transfer function calculation between the stress and the strain/displacement waveforms. Estimation of the elastic modulus from the displacement transfer functions is described in [11] and is repeated in Appendix B using the strain transfer functions.

C. Power-Law Effect

It is known that human soft tissue and most tissue mimicking phantoms behave like non-Newtonian fluids in the presence of a dynamic excitation. Newtonian fluids, like water, preserve their elastic and viscous properties at all frequencies, but non-Newtonian materials exhibit different elastic and viscous properties at different frequencies. In most materials, the variation in viscosity versus frequency can be modeled by a power-law [34]. For a generalized power-law fluid, the viscosity can be expressed as:

$$\eta = \eta_c \omega^n, \quad (3)$$

where η_c is the consistency index, ω is the angular frequency, and n is the flow index. For Newtonian fluids, $n = 0$. The case of $n > 0$ is rarely encountered in biological tissues and is referred to as dilatancy or the shear-thickening effect. The case of $n < 0$ is known as the shear-thinning or pseudo-plastic effect and is very common in polymers and gelatin composites. Accounting for the power-law effect in viscosity is a special case of the Kelvin-Voigt fractional derivative model of the viscoelasticity, which was used previously to model the response of canine tissue over a wide frequency range [29].

III. ALGORITHMS

The magnitude and phase of the transfer functions depend on the elastic and viscous properties of the medium. To show how transfer functions between the strains and the applied stress change as an inclusion appears in the medium, a four-element network of mass-spring-dampers is simulated. The second element is assumed to have higher elasticity. The third element is assumed to have higher viscosity than the background. The density is assumed to be constant and equal to 1000 kg/m^3 . Figs. 2(a) and (b) show the values of elasticity and viscosity in the simulated medium. The model was excited for 10 seconds with 40 Hz low-pass filtered white Gaussian noise as the force and the displacements and strains were calculated. The transfer functions between the applied stress and the strains at every element were then computed and their magnitudes and phases are plotted in Figs. 2(c) and (d). The transfer functions were computed using blocks of 1 s with 75% overlap. Each curve in these two figures corresponds to the transfer function for one of the elements in the system. One can observe the change in the low-frequency asymptotes of the magnitudes due to different elastic properties. The phase change, however, follows a more subtle trend that can be associated with the ratio between the viscosity and elasticity. This ratio will be called the *tissue relaxation time* and can be reconstructed from the phase or imaginary part of the transfer functions. For the second element with a smaller relaxation time, the phase is closer to zero. For the third element with a larger relaxation time, the phase of the transfer function is larger. A small spatial drift in the phase at low frequencies results from the influence of inertia. Second order effects also can be seen in the transfer functions, causing the peaks in the magnitude plot and large variations in the phase plot at frequencies higher than 20 Hz.

A. Parameter Estimation

If the frequency is sufficiently small, the tissue motion will be governed only by its elastic properties, and the dynamic effects do not play a significant role. This is also evident from Fig. 2(c) in which the magnitudes of the transfer functions at low frequencies appear to be nearly flat. Thus, one can obtain an estimate for the elasticity of the medium from the low-frequency asymptotes of the transfer functions [11], [12], (see also Appendix B).

The phase change in the transfer function is due to both elasticity and viscosity variations. As seen in Fig. 2, the phases of the transfer functions change considerably when an inclusion occurs in either the viscosity or the elasticity. It is shown in Appendix A that the transfer function between the local strain and the applied stress can be parameterized in terms of the Voigt model parameters as follows:

$$H_\sigma^\epsilon(\omega) = \frac{1}{(\mu + j\omega\eta)}. \quad (4)$$

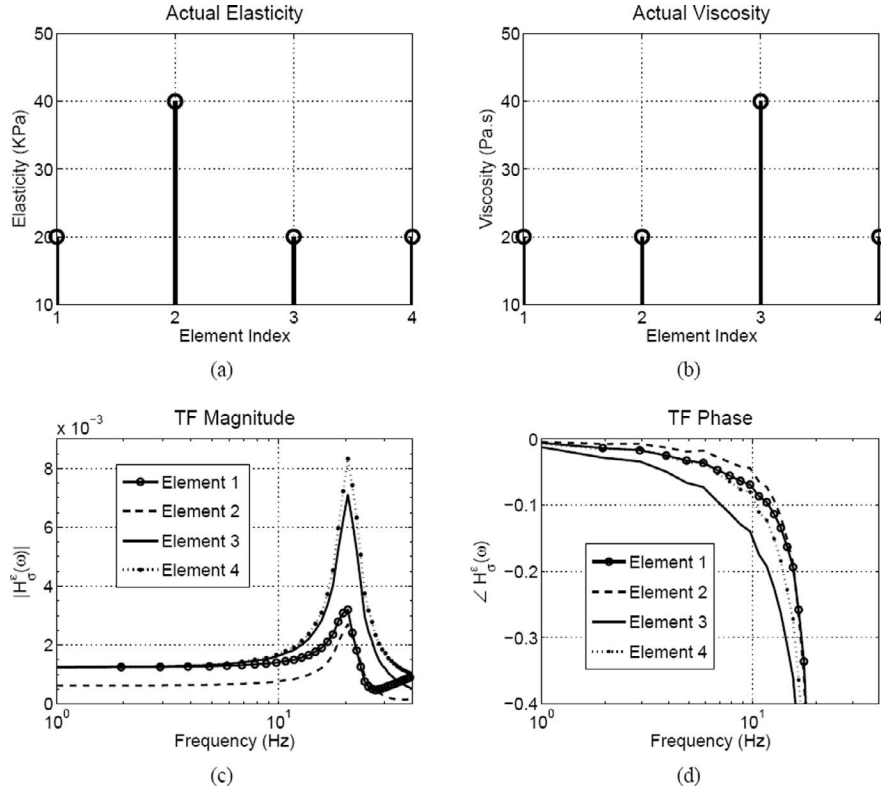


Fig. 2. The effect of changing the viscoelastic parameters on the transfer functions. (a) and (b) Show the elasticity and the viscosity of a four-element 1-D simulated phantom. (c) and (d) The magnitude and phase of the transfer functions (TF) between the strains at the applied stress. The excitation force was white noise, low-pass filtered at 40 Hz.

Assuming $\omega\eta$ is much smaller than μ , it follows that:

$$\frac{\omega\eta}{\mu} \approx -\angle H_{\sigma}^{\epsilon}(\omega). \quad (5)$$

The above equation shows that a high viscosity region affects the phase in the same way as a low elasticity region. Although one can estimate the viscosity by calculating η from (5), it is more straightforward to define and estimate a relaxation time (τ) for viscoelastic tissue as follows:

$$\tau = \frac{\eta}{\mu} \approx -\frac{1}{\omega} \angle H_{\sigma}^{\epsilon}(\omega). \quad (6)$$

A large τ indicates a slow response for the corresponding element. This is equivalent to the group delay of the transfer function at that frequency, considering that the phase changes linearly versus frequency.

If the viscosity has a power-law trend and elasticity is independent of frequency, the relaxation time will be subject to a similar behavior. The distribution of the flow index resulting from the power law in the relaxation time will thus yield another tissue parameter to be identified. If this power-law trend is ignored, the relaxation time can be assumed constant in a frequency range that inertia does not interfere. Therefore, instead of dealing with a single frequency, the slope of the phase with respect to frequency in (6) can be calculated to obtain a robust estimate of the relaxation time.

If the stress is unknown, the transfer functions can be computed with respect to the strain at a specific location.

Hence, (15) from Appendix A can be used to derive the following estimate for the distribution of relaxation time:

$$\hat{\tau} = \tau_0 - \frac{1}{\omega} \angle H_{\epsilon_0}^{\epsilon}(\omega), \quad (7)$$

where $\tau_0 = \eta_0/\mu_0$ is the relaxation time for the element of reference. Because τ_0 is unknown, it can be eliminated from (7) by assuming it to be constant. Although this is a biased estimate, the bias is constant for all of the elements and is equal to τ_0 . Therefore, the above equation gives a relative but correct profile of the distribution of the relaxation time in the tissue. However, the power-law effect cannot be seen readily here without measuring the force. If the power-law behavior is ignored, $\hat{\tau}$ can be averaged at several frequencies to obtain more robust estimates.

In order to quantify the estimation error, the stress is assumed to be known in the simulations in Section IV. However, the experimental data in Section V do not include any force measurement, thus relative estimates are presented.

IV. SIMULATIONS

In order to investigate the accuracy and noise sensitivity of the proposed methods, 1-D finite-element simulations were performed. The system in Fig. 1 was constructed with 100 elements. A band-limited force was applied and the displacements were computed. The details on how to

simulate a mass-spring-damper network are presented in Appendix C.

The model was assumed to represent a cross-section of 1 mm² and a depth of 50 mm of the tissue. The medium was homogeneous with the elasticity of 20 kPa and viscosity of 20 Pa·s. These values were chosen arbitrarily in the range of the viscoelastic properties for average soft tissues. The density of the phantom was 1000 kg/m³, which is equal to the density of water and most soft tissues. The simulation frame-rate was 1 kHz and the duration of each test was 10 seconds. The applied stress was white noise, low-pass filtered at 30 Hz. The simulated model was linear; hence, the magnitude of the applied force would not cause any nonlinear effects in the displacements, nor would it change the estimation results. The maximum strain that was observed in the phantom was no more than 1%. The displacements were computed at each node and the transfer functions were calculated between the strains and the applied stress.

Using (17) and (7), relative estimates for elasticity and relaxation time were calculated. For the simulated homogeneous phantom, the parameter estimates for all of the elements are expected to be equal; thus a high standard deviation indicates poor estimation. If p_0 is the actual value of the parameter and the vector \hat{p} is the estimate for all of the elements, the estimation error (Er_e) can be defined from the standard deviation (STD) as follows:

$$Er_e = \frac{\text{STD}(\hat{p})}{p_0}. \quad (8)$$

The sensitivity of the estimations to the noise level can be measured by calculating Er_e under the assumption that the displacements are noisy. Therefore, the model was simulated, and the actual strains were calculated. A certain level of noise then was added to the strains, and the transfer functions were calculated using the noisy strain data. This noise is meant to account for the quantization error and limited resolution in the displacement estimation, interference of the lateral motion of the tissue in the axial motion tracking, nonlinearities in the tissue, and imperfections of the model. A white Gaussian noise model has been assumed to address the sum of these sources of error. A more detailed study of the displacement and strain noise distribution is beyond the scope of this paper, but it has been investigated by others [35]. A simple noise model has been adopted in order to compare the effects of various parameters on the accuracy of the estimation, rather than precise quantification of the error.

The accuracy of the proposed methods are evaluated for a wide range of strain signal-to-noise ratios (SNR). For each level of the added noise on the strain data, 100 simulations were performed. The accuracy of the elasticity and relaxation-time estimations were calculated each time using (8), and the results were averaged for all of the 100 instances. Fig. 3 shows the Er_e for the elastic modulus and the relaxation time. The elasticity was reconstructed from the low-frequency asymptote of the transfer functions magnitudes. The relaxation time was calculated from

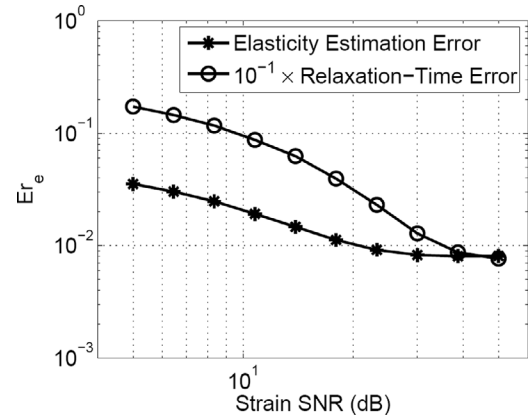


Fig. 3. The error in estimating the elasticity (star markers) and the relaxation time (RT, circle markers) for different levels of SNR of the strain. The error has been calculated based on the deviation of the estimates from the actual value of that parameter. Note that the estimation error for the relaxation time is divided by 10.

the phase, averaged between 2–10 Hz as described in Section III-A. The estimation error for the relaxation time has been divided by 10 in order to clearly display both curves in the same figure.

The strains in the previous calculations were computed by taking the derivative of the displacements. Alternatively, one can use the least-squares (LSQ) technique to calculate the gradient of the displacement that will reduce estimation variance at the cost of reduced contrast [36]. The effect of the LSQ kernel size on the estimation error is illustrated in Fig. 4(a). The network was simulated with 100 elements. The first 50 elements had a background elasticity and relaxation time equal to 20 kPa and 2 ms, respectively. The values for the second 50 elements in the network were 40 kPa and 1 ms. The strain was assumed to have a finite SNR of 15 dB. The LSQ kernel size was increased from 2 points, which is the discrete derivative, to 15 points, which corresponds to 7.5 mm in the tissue. For as many as 100 tests, Er_e was calculated for the first half and the second half of the region separately, and the results were averaged. It can be seen that increasing the LSQ kernel size reduces the estimation variance for both elasticity and relaxation time. Note that the increase in the average background parameters compared to the results in Fig. 3, marginally enhances the estimation accuracy. Fig. 4(b) shows the effect of the LSQ kernel size on the contrast-to-noise ratio (CNR) for the two-layered simulated phantom. The CNR is defined as follows:

$$\text{CNR} = \frac{2(M_1 - M_2)^2}{\text{STD}_1^2 + \text{STD}_2^2}, \quad (9)$$

where M_1 and M_2 are the means and STD_1 and STD_2 are the standard deviations of the estimated parameter at the two regions [35]. A large difference in mean values or very low noise levels can result in high CNR. The CNR resulting from the relaxation time is multiplied by 10 to show both curves in the same figure. In the experimental studies that will be presented in the following section,

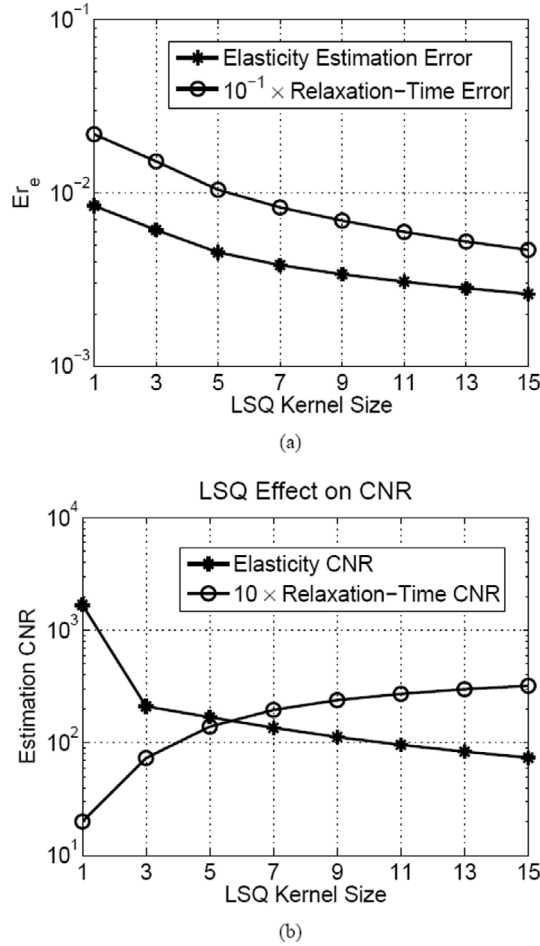


Fig. 4. The effect of the LSQ kernel size on the estimation. These are calculated using a two-layered simulated phantom. (a) The estimation error E_{re} for elasticity and relaxation time decrease as a wider LSQ kernel is applied. (b) The effect of the LSQ kernel size on the CNR.

an LSQ filter with an appropriate kernel size is used to achieve better noise rejection. Note that, for these tests, the frequency ranges used for the estimations were kept unchanged to maintain consistency. However, in practice, finding a proper frequency range will be crucial to obtaining good parameter estimates and, therefore, contrast.

V. EXPERIMENTS

The proposed methods were tested on tissue-mimicking phantoms. Special hardware and software were implemented for controlled tissue excitation and data acquisition. The experimental setup, phantom construction technique, and experimental results are described next.

A. Actuator and Rheometer Design

The schematic of the experimental setup is shown in Fig. 5. The design consists of an immobile platform that seats the actuation system, sensors, and the transducers. The motion of the vibrating stage is guided by a linear

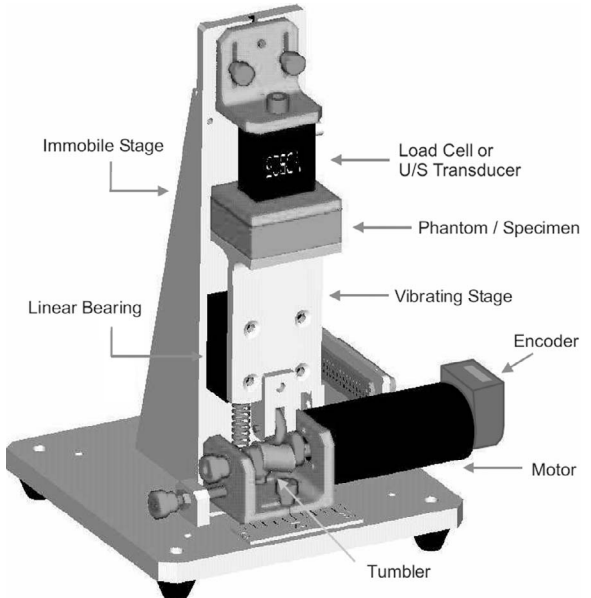


Fig. 5. The schematic of the experimental setup. The ultrasound probe is held stationary while a DC motor moves a stage and causes the phantom to be compressed.

bearing and preloaded by a spring from the bottom to maintain contact between its wheel and a motor-driven tumbler. The linear bearing is actuated by a coreless direct current (DC) motor (#118778, Maxon Motor, Sachseln, Switzerland) with a “tumbler”, a cylinder mounted obliquely on its shaft. The angled cylinder acts like a continuously variable elliptical cam. The amplitude is manually adjusted by moving the motor in the transverse direction. An incremental encoder with 1000 cycles per revolution (Type E2 from US Digital, Vancouver, WA) was mounted on the motor shaft for position feedback. The motion of the vibrating stage with respect to the static section is monitored by a position sensing device (PSD) that tracks the light spot of a small infrared, light-emitting diode (IR-LED). The PSD signal was used to validate the motion tracking methods and to control the average strain in the phantom. A 1-D PSD (type S3932, Hamamatsu Photonics K.K., Hamamatsu City, Japan) together with the required circuitry was mounted on the static part and the IR-LED was connected to the vibrating stage. The control of the motor, as well as the required data acquisition, was done on a computer using a PCI interface card and a terminal board (Q8, Quanser Inc., Markham, ON, Canada).

A real-time program was developed using WinCon (by Quanser) and Simulink (Mathworks, Inc., Natick, MA) to generate the desired waveforms. A velocity-control feedback loop was established between the signal recorded from the encoder and the waveform applied to the motor. The user can either specify a frequency of rotation, which would apply continuous, full-rotary motion to the motor, or generate any desired wide-band excitation, which would cause the tumbler to oscillate without making complete turns. In the former case, the transverse position of the tumbler determines the vibration amplitude. In the latter case, the

power of the generated waveform determines the amplitude of vibration.

The device can be used either as a rheometer or as an ultrasound vibro-elastography system. When used as a rheometer, a compression load-cell (Transducer Techniques, Temecula, CA) is mounted on the stage and a small material sample is placed between the vibrating plate and the load-cell. An oscillation with a specified frequency and amplitude is applied, and the force and displacement are recorded from the load-cell and the PSD, respectively. Precise knowledge of the actual dimensions of the specimen is necessary to calculate the exact values of the elasticity and viscosity. However, the relaxation time can be determined independently from the sample dimensions and can be recovered from the phase difference between the force and the position signal using (7). Note that the stress and the force have the same phase, and there is only a scaling factor between them equal to the cross section of the sample. Also note that the position recorded from the PSD can be divided by the length of the sample to obtain the average strain. Therefore, the transfer function phase in (7) can be substituted simply by the phase of the transfer function between the force and the PSD position signal.

When the device is used for vibro-elastography, a linear array ultrasound transducer is mounted in an aluminum case and attached to the stage. A phantom is placed on the vibrating plate and is pressed against the ultrasound probe on top of it, using ultrasound coupling gel. In this way, a desired excitation can be applied to the motor, and the motion within the phantom can be monitored using ultrasound motion estimation techniques. Sequences of radio frequency (RF) data frames can be recorded using a Sonix RP ultrasound machine (Ultrasonix Medical Corp., Richmond, BC, Canada). For the experiments reported, the recorded ultrasound RF lines have a center frequency of 5 MHz and were sampled at 20 MHz. After the acquisition, the A-lines were up-sampled by a factor of three to increase the accuracy in measuring the displacements. The acquisition frame-rate depends on the number of lateral A-lines in the imaging window. The axial displacements are estimated using a time-domain, cross-correlation technique with prior estimates [37]. The correlation coefficients were monitored to ensure accurate motion tracking. The frame of reference for motion tracking was changed only when the average of the correlation coefficients had a significant drop (i.e., below 85%). Thereby, the displacement estimation drift was minimized and higher accuracy was achieved at low frequencies. Depending on the experiment, the kernel size and overlap can be adjusted; however, for a typical experiment that will be described in the next section, they were held constant at 1.5 mm and 40%, respectively.

B. Phantom Construction and Rheometry

To construct a phantom with a significant contrast in the relaxation time, a small piece of PVA sponge (Ceiba Technologies, Chandler, AZ) was embedded in a cubic gelatin phantom. This type of sponge exhibits a signifi-

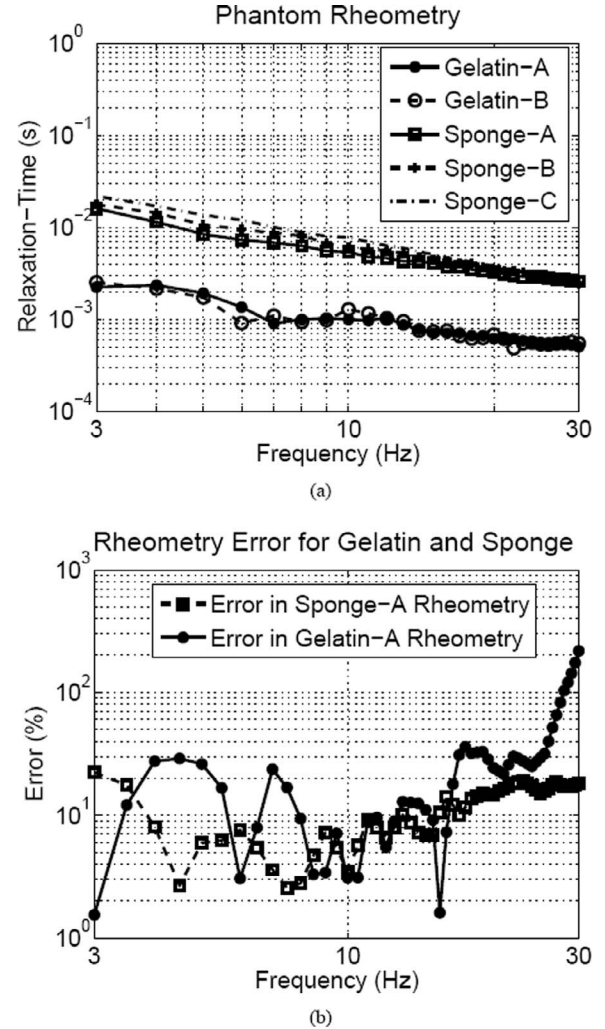


Fig. 6. (a) Relaxation-times of the PVA sponge and soft and hard gelatin phantoms versus frequency. Gelatin-A and gelatin-B are soft and hard gelatin phantoms, respectively. Sponge-A is the squeezed PVA sponge after it has been soaked in water, sponge-B is the partially squeezed sponge, and sponge-C is the wet PVA sponge instantly after being removed from the water. The relaxation times for the soft and hard gelatin are almost the same, and that of the sponge is higher by about one order of magnitude. (b) Shows the errors in measuring the relaxation times of the sponge and gelatin with respect to the data from a stress-controlled rheometer.

cantly different viscosity than the gelatin. One can investigate the difference between the relaxation times in the sponge and gelatin through simple palpation by observing the recovery times. To measure the exact relaxation times, a piece of sponge and a soft and a hard sample of gelatin phantom were examined using the aforementioned rheometer. The hard gelatin phantom was approximately three times harder than the soft one. Fig. 6(a) shows the relaxation times versus frequency. The sample dimensions were the same, having 3-mm thickness and 20-mm × 12-mm surface area. The relaxation time of the PVA sponge was measured in three different states. First, the test was performed instantly after the sponge was removed from the water. Then, the sponge was partially compressed and the test was repeated. Complete compression was applied

to the sponge to remove the existing water drops and another measurement was taken. The force and the position were recorded and the relaxation time of the material was estimated as described in Section V-A. It can be seen in Fig. 6(a) that the two gelatin samples have approximately the same relaxation times, but that of the sponge is significantly higher. The decreasing trend in the curves with respect to the frequency is due to the power-law effect. These results also have been validated by shear rheometry using a commercial, stress-controlled rheometer (Bohlin C-VOR, Malvern Instruments Ltd., Worcestershire, UK). Using the generalized Hook's law and the assumption of incompressibility of the material, it can be shown that rheology with both rheometers should yield the same value for the relaxation time. Fig. 6(b) shows the relative error of the measured relaxation times with respect to the results from the Malvern rheometer. Compared to the rheometry validation results, the curves in Fig. 6(a) have 20% and 12% deviation for the soft gelatin and wet sponge, respectively. Note that the experiments with both rheometers have variability that depends on experimental conditions that may account for the higher error at high frequencies in Fig. 6(b).

The gelatin phantom was made using bovine skin gelatin (type G9382-B, Sigma-Aldrich Inc., Oakville, ON, Canada) in water and 2% cellulose (by weight) as the scatterers. The phantom dimensions were 65-mm axially, 55-mm laterally, and 35-mm elevationally. The sponge sample, having been soaked in water and compressed periodically over the course of several weeks to remove all air bubbles, was embedded in the gelatin immediately after being removed from the water. The speed of sound in the wet sponge was approximately 1600 ms^{-1} , which is close to that of water. However, the attenuation of the ultrasound in the sponge was considerably higher than that in gelatin, which can be explained by the high viscosity of its constituent material. Hence, a thin sample was cut for the experiments to ensure good quality in the RF A-lines without shadowing. For fully developed ultrasound speckle, the amplitude distribution of each RF frame should have a Rayleigh distribution with a ratio of mean over standard deviation equal to 1.9 [38]. For the case in which the phantom was held stationary, this parameter was 1.91 for all of the frames. This indicates that the recorded A-lines had fully developed speckle distributions, so standard tracking algorithms are used.

C. Data Analysis and Results

The transfer functions are computed for all of the strains on each line with respect to the strain of an arbitrary block in the middle of that line. The coherence functions are also calculated to ensure the linearity of the tissue response. A high coherence function (i.e., close to one) indicates that the input-output relation is linear and the noise is small [39]. If the applied stress is known, the coherence function between the stress $\sigma(t)$ and the strain $\epsilon(t)$ at some location in the phantom is:

$$C_{\sigma}^{\epsilon}(\omega) = \frac{|P_{\epsilon\sigma}(\omega)|^2}{P_{\sigma\sigma}(\omega)P_{\epsilon\epsilon}(\omega)}. \quad (10)$$

In the presence of noise and nonlinearities, the coherence values likely decrease as the input power level increases [40]. In elastography experiments, this may be due to the larger lateral motion in the phantom or sources of nonlinearities in the tissue such as the effect of large strain and hysteresis.

In the first test, the gelatin part of the phantom contained 18 wt.% gelatin powder. A high gelatin concentration was used in order to reduce the elasticity contrast between the sponge and the gelatin. A small piece of PVA sponge (5-mm thick) was placed in the middle of the gelatin phantom, approximately 13 mm away from the probe face. The phantom was excited with Gaussian white-noise, band-limited to 3–30 Hz. The standard deviation of the Gaussian distribution was $80 \mu\text{m}$, and the average strain applied to the phantom was no more than 0.3%. RF-lines were collected for 60 seconds at 1300 frames/second in the Doppler mode from a single A-line passing through the sponge. The imaging window length was 40 mm extending from the probe face. The displacements were estimated with 70 blocks of 1.5 mm each with 40% overlap between them. The accuracy of the displacement estimates can be verified by examining the correlation coefficients [41]. The histogram of the correlation coefficients at all the blocks for the duration of the experiment is shown in Fig. 7(a), exhibiting an average of 99.4%. To ensure faster motion tracking, stretching has not been applied to the compressed RF signals. However, the high correlation coefficients obtained indicate that the accuracy was well preserved in the results. The spectrum of the displacement of a typical block at 30 mm from the probe is shown in Fig. 7(b). The spectrum of the PSD measurement also is shown on the same plot. The coherence function between this nodal displacement and the PSD signal is shown in Fig. 7(c). The high coherence within the excitation frequency range indicates that the estimated displacements accurately follow the position measured by the PSD. The strain was calculated at every time-step with a 7-point LSQ filter that corresponds to 4 mm in the tissue. The transfer and coherence functions for the strains were calculated using blocks of 1 second with 50% of overlap. The reference block to compute the transfer functions was element 30, in the middle of the phantom, with high-correlation coefficients in its vicinity. Any other node with high correlation coefficients is an acceptable choice as the reference. The magnitude and the phase of the transfer function for element 18 at 10-mm depth are shown in Fig. 7(d). Note that the transfer functions are acceptable only at 3–30 Hz. Beyond this frequency range, the coherence functions drop, and the spectral estimations would be inconsistent. The coherence functions between the local strains and the strain at the reference block had an average of 0.98 within the excitation frequency range. This indicates the high linearity of the tissue response. Higher coherence values result for the nodes closer to the probe, due to the drop in ultra-

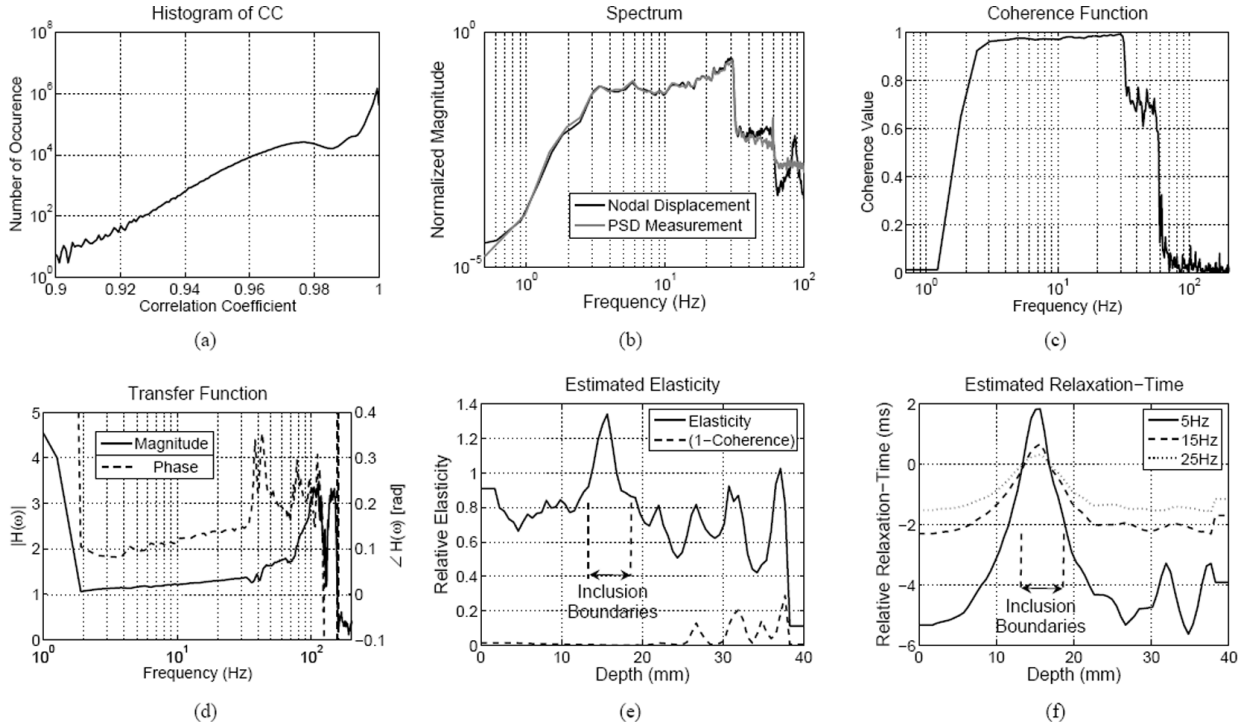


Fig. 7. Single-line data acquisition and parameter estimation in a gelatin phantom with a PVA sponge inclusion and excited at 3–30 Hz. (a) Histogram of the correlation coefficients. (b) Normalized spectrum of the displacement of a node at 30 mm (black line) and the spectrum of the measurement from the PSD (gray line). The coherence function between these two signals is shown in (c). The magnitude and phase of a sample transfer function between element 18 and 30 are shown in (d). The reference element 30 is located at a depth of 17 mm. (e) The elasticity estimates from the asymptotic magnitude of the transfer functions. The values are normalized with respect to the elasticity of the reference element. The error in estimation is depicted as one minus the value of the coherence function at each point. (f) The relaxation time estimates from the phase of the transfer functions at three different frequencies. Again, the values are the difference between the actual relaxation time of the phantom and the relaxation time of the reference element at a depth of 17 mm. The inclusion boundaries are delineated in both figures.

sound power and resolution with depth and lower motion tracking accuracy for deeper nodes. The estimation of the elasticity, using the asymptotic magnitude of the transfer functions, is shown in Fig. 7(e) and the relaxation-time estimates from the phase of the transfer functions at three different frequencies are plotted in Fig. 7(f). It can be seen in Figs. 6(a) and 7(f) that the contrast between the relaxation times of gelatin and sponge decreases as the frequency is increased. The error in estimation is shown as one minus the value of the coherence function at each point. A low coherence function indicates nonlinearity of the response or a high amount of noise in the data. A coherence value of nearly one, indicates the validity of the linear model. Note that the elasticity estimates are normalized with respect to the unknown elasticity of the reference element (element 30 at a depth of 17 mm) and the estimated relaxation time of each element is the actual relaxation time minus the relaxation time of the reference element, which also is unknown.

In another experiment, a soft gelatin phantom (12 wt.% gelatin in water) was constructed with two inclusions inside it. One inclusion was a hard cylinder of the same gelatin material (18 wt.% gelatin in water), approximately 2.5 times stiffer than the background. The other inclusion was a small piece of PVA sponge, saturated with water. Multiple A-lines were captured over the region of interest

at 98 frames/second for a duration of 20 seconds. The dimensions of the phantom, excitation characteristics and the displacement estimation parameters were the same as in the previous experiment. The imaging window was 40 mm × 40 mm with 64 RF-lines in the lateral direction. The 1-D displacements were estimated with 70 blocks for all the lines, resulting in an average of 98.6% for the correlation coefficients. The strains were calculated with a 4-mm LSQ filter. The transfer functions were calculated for the strain of each line with respect to an element close to the probe (element 5), using the same parameters as the previous experiment. The coherence values had an average of 0.9 within the frequency range of excitation. In order to remove possible outliers and present a clear image of the estimated parameters, a 5 × 5 pixels median filter was applied to the images. The low-frequency asymptotes of the transfer functions between 3–10 Hz were used in order to estimate the relative value of the elasticity in the phantom. Fig. 8(b) shows the estimated elasticity, which clearly delineates a hard inclusion at the middle left and another one at the middle right of the phantom. The left-side inclusion is the hard gelatin and the right-side inclusion is the sponge. The relaxation time was estimated from the phase of the transfer functions at 15 Hz and is shown in Fig. 8(c). The difference between the relaxation times of the gelatin and the sponge is apparent in this image.

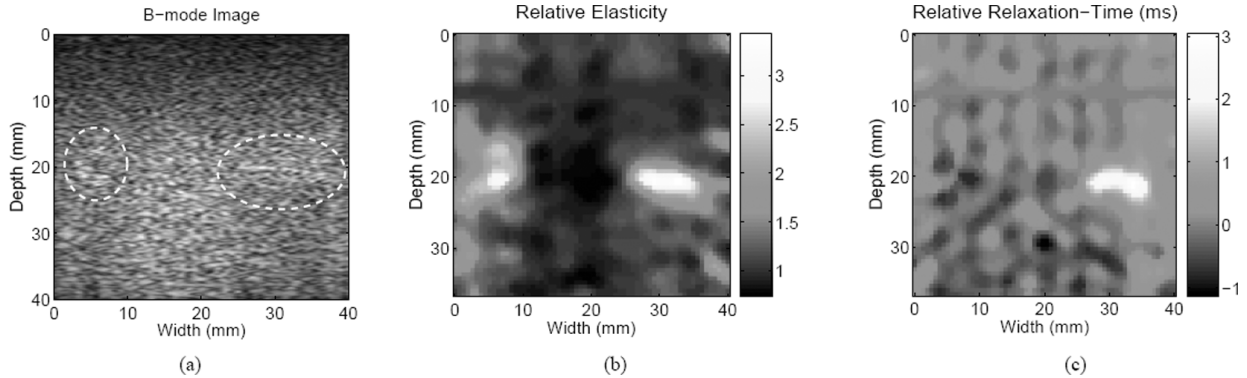


Fig. 8. Estimated parameters for a gelatin phantom (12 wt.% in water) with a hard gelatin (18 wt.% in water) inclusion at the middle left and a PVA sponge inclusion at the middle right. The inclusions are delineated in the B-mode image (a). The inclusions are not easily detectable in the B-mode image but they are known to be within the dashed ellipses. The elasticity estimate of the phantom can be used to detect both inclusions (b). The low-frequency asymptotes of the transfer functions between 3 Hz and 10 Hz were used. Note that both inclusions appear as harder regions in the elasticity image. Although elastic modulus does not provide a contrast between the hard gelatin and sponge inclusions, the relaxation-time estimate in (c) can distinguish the sponge in the gelatin environment. The phase of the transfer functions at 15 Hz was used to calculate relaxation time. As expected from rheometry, the relaxation times of the soft and hard gelatin materials are nearly the same, but sponge has a significantly different relaxation time.

TABLE I
POWER-LAW FIT OF RELAXATION TIME FOR THE PVA SPONGE AND GELATIN.

	η_c/μ [ms]	n
Gelatin-A	4.6	-0.66
Gelatin-B	4.5	-0.65
Sponge-A	29.2	-0.73
Sponge-B	43.9	-0.84
Sponge-C	62.9	-0.94

VI. DISCUSSION

The simulations and phantom experiments demonstrate the feasibility of reconstructing the relaxation time in order to distinguish different soft tissues. The elasticity and the relaxation time were both estimated using a frequency analysis of the tissue response. Although using a transfer function approach eliminates the need for a specific tissue model, a linear viscoelastic model has been used to verify the algorithms.

The rheometry experiments reveal the difference between the relaxation times for the gelatin and the PVA sponge. From Fig. 7(f), the difference between the relaxation times of the gelatin and sponge is smaller at 15 Hz and 25 Hz than at 5 Hz in Fig. 7(f). The decrease in the relaxation time is governed mainly by a power law that is evident in Fig. 6(a). However, unless the force is measured or the parameter τ_0 (the relaxation time of the reference element) in (7) is known, this power law cannot be deciphered with the current approach. Table I contains the consistency index (η_c/μ) and the flow index (n) of the best power-law fit for each relaxation time curve extracted from the data in Fig. 6(a). The consistency index explains the higher relaxation time of the sponge compared to the

gelatin and the index n describes the higher negative slope of the curves pertaining to the PVA sponge. Both parameters, if successfully estimated, could be suitable features for distinguishing different materials in phantoms and likely in human tissue. Note that here, the elasticity is assumed to be independent of frequency. In this way, the flow index of the viscosity would be the same as that of the relaxation time. However, it is shown in [34] for some animal tissue that the elasticity increases slightly as the frequency is increased. As a result, the flow index for elasticity, viscosity, and relaxation time would be different.

According to the rheometry results in Fig. 6(a), the difference between the relaxation times of the sponge and the gelatin at 5 Hz, 15 Hz, and 25 Hz are approximately 11 ms, 4.3 ms, and 2.4 ms, respectively. This difference was estimated to be 7.7 ms, 3 ms, and 1.8 ms, respectively, at those frequencies based on the estimation results depicted in Fig. 7(f). Considering that using an LSQ filter in the estimations reduces the contrast, the parameter estimation and the rheometry data seem to match reasonably well. Fig. 8(c) estimates this difference in relaxation time to be approximately 3 ms, which also agrees with the rheometry.

The presence of tissue harmonics at about 30 Hz in the simulations had a large effect on E_{re} . Although the system was simulated by second order mass-spring-damper elements, identification was performed by fitting a first order Voigt model to each element. As a result, the error should be larger for higher frequencies of excitation. This problem was not encountered in the experiments. A first order system could be fit accurately to the transfer functions, and the effect of inertia could be ignored at the frequencies below 30 Hz.

In the experiments, a band-limited force has been applied to the phantom. Fig. 7(b) shows that most of the excitation power is in the range of 3–30 Hz. However, a significant 60 Hz interference can be seen in the recorded

signal from the PSD, which is due to the cross-talk with the power lines and the oscillations in the ambient light. The limited resolution of the PSD accounts for the noise level at higher frequencies. There is also a noticeable peak in the spectrum of the estimated displacement at 86 Hz and a few smaller peaks at higher frequencies. This peak, which was not in the excitation and is not present in the PSD spectrum, is likely from the harmonic vibrations of the tissue. This identifies the frequency at which the inertia starts to interfere in the spectrum. Some excitation power is also seen in the range of 30–60 Hz that is due to the particular shape of the tumbler, producing a nonlinear transform between the rotation of the motor shaft to the motion of the stage. As a result, Fig. 7(c) shows coherence values of about 0.7 at this frequency range, but this range was not used for analysis.

In the single A-line experiment, the relaxation time seems to have higher contrast and a smoother profile compared to the elasticity. This is expected as the phantom was designed to have a stiffness close to that of the PVA sponge. The relatively high elastic modulus of the gelatin may have caused a nonhomogeneous sol-gel transition at the time the phantom was made, which can account for the presence of large local variations in the elasticity of the phantom. The other reason for the high variance of the elasticity and the relaxation time at the depth interval of 25–40 mm in Fig. 7 is the lower correlation coefficients resulting from the displacement estimation at that section of the phantom. The average correlation coefficients for the first and second halves of the phantom are 99.9% and 98.9%, respectively. Considering the high frame rate of 1,300 Hz and the small compression between consecutive frames, the second half of the phantom exhibits relatively small correlation coefficients. Higher lateral motion, poorer quality of the RF A-lines as a result of high attenuation in the sponge, or higher axial motion and signal decorrelation in the phantom might be the sources of the degraded motion tracking at that region.

In Fig. 4(a), it is shown that using an LSQ filter improves the estimation for both elasticity and relaxation time. This was expected because the least-squares filter gives a smooth approximation of the derivative at the cost of contrast. It raises the question of what is the appropriate LSQ filter size. The contrast of the elasticity estimate drops by increasing the LSQ kernel size, but the relaxation time estimation does not seem to suffer from this trade-off. In the range that is shown in Fig. 4, the relaxation-time CNR increases as the filter size is increased, so it may be desirable to increase the LSQ filter length to achieve lower estimation error and higher CNR for the relaxation time. As a trade-off, increasing the filter length limits the resolution and lowers the ability to detect small inclusions. It also should be noted that an extremely wide LSQ filter eventually decreases the CNR of the relaxation time estimates.

Besides the quantitative analysis of a 1-D experiment depicted in Fig. 7, the same technique has been extended to a 2-D image in Fig. 8, using several 1-D estimations.

Therefore, the parameters have been separately estimated in each line, then the images were formed by joining the individual lines together. Fig. 8 shows that the elasticity of both inclusions are higher than the background, and the relaxation time is higher only for the sponge. These results show that the relaxation time, as a dynamic parameter in the tissue, can be used as a complementary feature to elasticity to distinguish between different soft tissues.

In an ideal case, all the components of the displacement tensor and their spatial derivatives are used to reconstruct the 3-D distribution of the mechanical parameters in tissue. As proposed recently [42], the deformations due to a shear excitation can be more accurately reconstructed in 3-D by imaging the tissue motion ultrasonically from several angles. Although such a method, being capable of solving the wave equation in 3-D, can be very promising, it requires the subject to remain still for a few minutes during the examination. The estimation of the parameters (especially the dynamic ones) also will require accurate synchronization between the imaging transducer and the excitation at different angles. The simplicity that the linear 1-D model in the present work offers makes possible the real-time viscoelastic parameter estimation in soft tissue with a simple excitation scheme. The shortcomings of a 1-D model of deformation can be compensated by its advantages in terms of a short period of examination, high-computational speed, and relative ease of implementation.

VII. CONCLUSIONS

It is feasible to estimate the viscoelastic properties of a material by vibrating over a range of low frequencies and analyzing the time series of motion measurements at multiple locations. This can be performed by calculation and analysis of transfer functions in the frequency domain. From the phase of the transfer functions, the property of relaxation time can be measured. The relaxation time is proposed as a potential complementary feature to elasticity to distinguish materials with different mechanical properties. The errors of the algorithm have been quantified through computer simulations. The apparatus for testing these concepts on tissue-mimicking phantoms was described and used to investigate the key factors affecting accuracy. The relaxation times of different phantom materials were measured successfully. The accuracy of the measured relaxation times was found to be dependent on appropriate filtering in the strain calculations, suitable frequency range of excitation, and an understanding of the non-Newtonian behavior of the material. The viscosity of the material was modeled with the power-law and the model parameters determined by rheometry. The model parameters calculated from rheometry were similar to the parameters calculated with the transfer functions. Overall, the transfer-function method shows promise for future work on measuring the viscoelastic properties of human tissue.

APPENDIX A TRANSFER FUNCTION PARAMETERIZATION

The constitutive equation of a Voigt element can be obtained in the frequency domain by taking the Fourier transform of (1):

$$(\mu + j\omega\eta)\epsilon(\omega) = \sigma(\omega), \quad (11)$$

where $\epsilon(\omega)$ is the Fourier transform of the strain at a specific location in tissue (any node in Fig. 1), and $\sigma(\omega)$ is the Fourier transform of the stress signal. μ and η are the local values of the elasticity and viscosity.

The transfer function between the strain and the stress is defined as:

$$H_\sigma^\epsilon(\omega) = \frac{P_{\epsilon\sigma}(\omega)}{P_{\sigma\sigma}(\omega)}, \quad (12)$$

where $P_{\epsilon\sigma}(\omega)$ is the cross-power spectral density between $\epsilon(t)$ and $\sigma(t)$ and $P_{\sigma\sigma}(\omega)$ is the power spectral density for $\sigma(t)$.

If stress has been recorded, (11) can be expressed as:

$$(\mu + j\omega\eta) = \frac{1}{H_\sigma^\epsilon(\omega)}. \quad (13)$$

Otherwise, the stress can be removed from (11) as follows:

$$(\mu + j\omega\eta)\epsilon(\omega) = (\mu_0 + j\omega\eta_0)\epsilon_0(\omega), \quad (14)$$

where μ_0 and η_0 are the parameters at any arbitrary location (along the 1-D line) and ϵ_0 is the strain at that point. By taking the transfer function between the strains at the two points, the following results:

$$\frac{(\mu + j\omega\eta)}{(\mu_0 + j\omega\eta_0)} = \frac{1}{H_{\epsilon_0}^\epsilon(\omega)}. \quad (15)$$

Different characteristics of the transfer functions, such as the magnitude and the phase, depend on the tissue properties. Identification of these mechanical properties from the transfer functions results in good estimates, because the amount of temporal averaging to calculate the power spectral density functions can be increased arbitrarily, and because the transfer function can be explored at several frequencies to extract a specific feature.

Instead of using the transfer function between the stress and the strain, one can use the applied force and the nodal displacements to calculate the transfer functions. From (2), the following results:

$$(k_i + j\omega b_i) = \frac{1}{H_f^i(\omega) - H_f^{i+1}(\omega)}, \quad (16)$$

where $H_f^i(\omega)$ denotes the transfer function between the force and the displacement at node i . The stiffness and the relaxation time can be calculated here, similarly to the case in which strains and stress are used to compute the transfer functions.

APPENDIX B ELASTICITY ESTIMATION

It has been shown in [11] that using (13), the following estimate for the elasticity can be obtained:

$$\hat{\mu} = \frac{1}{|\bar{H}_\sigma^\epsilon(\omega)|}, \quad (17)$$

where $\hat{\mu}$ is the estimated elastic modulus and $\bar{H}_\sigma^\epsilon(\omega)$ is the low-frequency asymptote of the transfer function. The term $j\omega\eta$ in (13) is ignored due to small frequency approximation and the fact that $\omega\eta \ll \mu$.

If the stress is not measured, (15) can be used to get the following relative estimate for the elasticity:

$$\hat{\mu} = \frac{\mu_0}{|\bar{H}_{\epsilon_0}^\epsilon(\omega)|}. \quad (18)$$

The estimates should be normalized with respect to μ_0 , which is unknown. Therefore, only the profile of the relative elasticity can be obtained.

APPENDIX C SIMULATING A MASS-SPRING-DAMPER NETWORK

The dynamic motion of the tissue can be described by a series of mass-spring-damper elements as depicted in Fig. 1. In such a network, the tissue motion is governed by the following equation [11]:

$$KX(t) + BX(t) + MX\ddot{X}(t) = F(t), \quad (19)$$

where $X(t)$ is the matrix that contains the displacements of all the nodes versus time and $F(t)$ is the external force. The matrices K , B , and M are the stiffness, damping, and mass matrices, defined in [11]. Therefore, a state-space model can be generated to compute the nodal displacement vectors:

$$\begin{aligned} \begin{bmatrix} \dot{X}(t) \\ \ddot{X}(t) \end{bmatrix} &= \begin{bmatrix} 0 & I \\ -M^{-1}K - M^{-1}B & 0 \end{bmatrix} \begin{bmatrix} X(t) \\ \dot{X}(t) \end{bmatrix} \\ &\quad + \begin{bmatrix} 0 \\ M^{-1} \end{bmatrix} F(t), \\ X(t) &= [I \ 0] \begin{bmatrix} X(t) \\ \dot{X}(t) \end{bmatrix}. \end{aligned} \quad (20)$$

The output, $X(t)$, can be numerically evaluated by direct discretization of the above model, using a fixed step-size. The Matlab function, *lsim*, has been used in this paper and the sampling frequency was fixed at 1 KHz.

ACKNOWLEDGMENT

The authors would like to thank Edward B. Muliawan and Professor Savvas Hatzikiriakos for their help with rheometry background and measurements using a stress-controlled rheometer.

REFERENCES

- [1] J. Ophir, I. Cespedes, B. Garra, H. Ponnekanti, Y. Huang, and N. Maklad, "Elastography: Ultrasonic imaging of tissue strain and elastic modulus in vivo," *Eur. J. Ultrasound*, vol. 3, pp. 49–70, Jan. 1996.
- [2] C. Pellet-Barakat, M. Sridhar, K. K. Lindfors, and M. F. Insana, "Ultrasonic elasticity imaging as a tool for breast cancer diagnosis and research," *Curr. Med. Imag. Rev.*, vol. 2, pp. 157–164, Feb. 2006.
- [3] R. M. Lerner, K. J. Parker, J. Holen, R. Gramiak, and R. C. Waag, "Sono-elasticity: Medical elasticity images derived from ultrasound signals in mechanically vibrated targets," in *Acoustical Imaging*, vol. 16, pp. 317–327, 1988.
- [4] J. Ophir, I. Cespedes, H. Ponnekanti, Y. Yazdi, and X. Li, "Elastography: A quantitative method for imaging the elasticity of biological tissues," *Ultras. Imag.*, vol. 13, pp. 111–134, Apr. 1991.
- [5] L. Gao, K. J. Parker, S. K. Alam, and R. M. Lerner, "Sonoelasticity imaging: Theory and experimental verification," *J. Acoust. Soc. Amer.*, vol. 97, no. 6, pp. 3875–3886, June 1995.
- [6] A. P. Sarvazyan, O. V. Rudenko, S. D. Swanson, J. B. Fowlkes, and S. Y. Emelianov, "Shear wave elasticity imaging: A new ultrasonic technology of medical diagnostics," *Ultrasound Med. Biol.*, vol. 24, no. 9, pp. 1419–1435, 1998.
- [7] M. Fatemi and J. F. Greenleaf, "Vibro-acoustography: An imaging modality based on ultrasound-stimulated acoustic emission," in *Proc. Nat. Academy Sci., U.S.A.*, June 1999, pp. 6603–6608.
- [8] J. Ophir, S. K. Alam, B. Garra, F. Kallel, E. Konofagou, T. Krouskop, and T. Varghese, "Elastography: Ultrasonic estimation and imaging of the elastic properties of tissues," *J. Eng. Med.*, vol. 213, no. H3, pp. 203–233, 1999.
- [9] K. Nightingale, M. Palmeri, R. Nightingale, and G. Trahey, "On the feasibility of remote palpation using acoustic radiation force," *J. Acoust. Soc. Amer.*, vol. 110, no. 1, pp. 625–634, 2001.
- [10] J. Bercoff, M. Tanter, and M. Fink, "Supersonic shear imaging: A new technique for soft tissue elasticity mapping," *IEEE Trans. Ultrason., Ferroelect., Freq. Contr.*, vol. 51, no. 4, pp. 396–409, 2004.
- [11] E. Turgay, S. E. Salcudean, and R. Rohling, "Identifying the mechanical properties of tissue by ultrasound strain imaging," *Ultrasound Med. Biol.*, vol. 32, no. 2, pp. 221–235, 2006.
- [12] S. E. Salcudean, D. French, S. Bachmann, R. Zahiri-Azar, X. Wen, and W. J. Morris, "Viscoelasticity modeling of the prostate region using vibro-elastography," in *Medical Image Computing and Computer-Assisted Intervention (MICCAI)*, vol. 4190, 2006, pp. 389–396.
- [13] R. Sinkus, M. Tanter, T. Xydeas, S. Catheline, J. Bercoff, and M. Fink, "Viscoelastic shear properties of in vivo breast lesions measured by MR elastography," *Magn. Reson. Imag.*, vol. 23, no. 2, pp. 159–165, 2005.
- [14] S. Chen, M. Fatemi, and J. F. Greenleaf, "Quantifying elasticity and viscosity from measurement of shear wave speed dispersion," *J. Acoust. Soc. Amer.*, vol. 115, no. 6, pp. 2781–2785, 2004.
- [15] S. Catheline, J. Gennisson, G. Delon, M. Fink, R. Sinkus, S. Abouelkaram, and J. Culioni, "Measurement of viscoelastic properties of homogeneous soft solid using transient elastography: An inverse problem approach," *J. Acoust. Soc. Amer.*, vol. 116, no. 6, pp. 3734–3741, 2004.
- [16] M. F. Insana, C. Pellet-Barakat, M. Sridhar, and K. K. Lindfors, "Viscoelastic imaging of breast tumor microenvironment with ultrasound," *J. Mamm. Gland Biol. Neoplasia*, vol. 9, pp. 393–404, Oct. 2004.
- [17] M. Sridhar, J. Liu, and M. F. Insana, "Viscoelasticity imaging using ultrasound: Parameters and error analysis," *Phys. Med. Biol.*, vol. 52, no. 9, pp. 2425–2443, May 2007.
- [18] J. Bercoff, M. Tanter, M. Muller, and M. Fink, "The role of viscosity in the impulse diffraction field of elastic waves induced by the acoustic radiation force," *IEEE Trans. Ultrason., Ferroelect., Freq. Contr.*, vol. 51, no. 11, pp. 1523–1536, 2004.
- [19] R. Sinkus, M. Tanter, S. Catheline, J. Lorenzen, C. Kuhl, E. Sondermann, and M. Fink, "Imaging anisotropic and viscous properties of breast tissue by magnetic resonance-elastography," *Magn. Reson. Med.*, vol. 53, pp. 372–387, Feb. 2005.
- [20] S. Girnyk, A. Barannik, E. Barannik, V. Tovstiak, A. Marusenko, and V. Volokhov, "The estimation of elasticity and viscosity of soft tissues in vitro using the data of remote acoustic palpation," *Ultrasound Med. Biol.*, vol. 32, no. 2, pp. 211–219, 2006.
- [21] W. F. Walker, F. J. Fernandez, and L. A. Negron, "A method of imaging viscoelastic parameters with acoustic radiation force," *Phys. Med. Biol.*, vol. 45, pp. 1437–1447, June 2000.
- [22] T. J. Hall, M. Bilgen, M. F. Insana, and T. A. Krouskop, "Phantom materials for elastography," *IEEE Trans. Ultrason., Ferroelect., Freq. Contr.*, vol. 44, no. 6, pp. 1355–1365, 1997.
- [23] E. L. Madsen, M. A. Hobson, H. Shi, T. Varghese, and G. R. Frank, "Tissue-mimicking agar/gelatin materials for use in heterogeneous elastography phantoms," *Phys. Med. Biol.*, vol. 50, no. 23, pp. 5597–5618, 2005.
- [24] R. Q. Erkamp, S. Y. Emelianov, A. R. Skovoroda, and M. O'Donnell, "Nonlinear elasticity imaging: Theory and phantom study," *IEEE Trans. Ultrason., Ferroelect., Freq. Contr.*, vol. 51, pp. 532–539, May 2004.
- [25] K. C. Chu and B. K. Rutt, "Polyvinyl alcohol cryogel: An ideal phantom material for MR studies of arterial flow and elasticity," *Magn. Reson. Med.*, vol. 37, pp. 314–319, Feb. 1997.
- [26] C. Joly-Duhamel, D. Hellio, and M. Djabourov, "All gelatin networks: 1. Biodiversity and physical chemistry," *Langmuir*, vol. 18, no. 19, pp. 7208–7217, 2002.
- [27] R. Sinkus, J. Bercoff, M. Tanter, J.-L. Gennisson, C. El-Khoury, V. Servois, A. Tardivon, and M. Fink, "Nonlinear viscoelastic properties of tissue assessed by ultrasound," *IEEE Trans. Ultrason., Ferroelect., Freq. Contr.*, vol. 53, pp. 2009–2018, Nov. 2006.
- [28] Y. C. Fung, *Biomechanics: Mechanical Properties of Living Tissues*. New York: Springer, 1993.
- [29] M. Kiss, T. Varghese, and T. Hall, "Viscoelastic characterization of in vitro canine tissue," *Phys. Med. Biol.*, vol. 49, pp. 4207–4218, Sep. 2004.
- [30] T. G. Mezger, *The Rheology Handbook*. 2nd ed. Norwich, NY: William Andrew, 2006.
- [31] J. S. Bendat and A. G. Piersol, *Engineering Applications of Correlation and Spectral Analysis*. 2nd ed. New York: Wiley-Interscience, 1993.
- [32] L. M. Brekhovskikh and V. V. Goncharov, *Mechanics of Continua and Wave Dynamics*. New York: Springer-Verlag, 1985.
- [33] H. Kolsky, *Stress Waves in Solids*. New York: Dover, 1963.
- [34] N. Phan-Thien, S. Nasseri, and L. Bilston, "Oscillatory squeezing flow of a biological material," *Rheologica Acta*, vol. 39, no. 4, pp. 409–417, 2000.
- [35] T. Varghese and J. Ophir, "An analysis of elastographic contrast-to-noise ratio," *Ultrasound Med. Biol.*, vol. 24, pp. 915–924, July 1998.
- [36] F. Kallel and J. Ophir, "A least-squares strain estimator for elastography," *Ultras. Imag.*, vol. 19, pp. 195–208, July 1997.
- [37] R. Zahiri-Azar and S. Salcudean, "Motion estimation in ultrasound images using time domain cross correlation with prior estimates," *IEEE Trans. Biomed. Eng.*, vol. 53, pp. 1990–2000, Oct. 2006.
- [38] R. Wagner, M. Insana, and S. Smith, "Fundamental correlation lengths of coherent speckle in medical ultrasonic images," *IEEE Trans. Ultrason., Ferroelect., Freq. Contr.*, vol. 35, pp. 34–44, Jan. 1988.
- [39] J. S. Bendat, *Nonlinear System Techniques and Applications*. New York: Wiley, 1998.
- [40] V. Z. Marmarelis, "Coherence and apparent transfer function measurements for nonlinear physiological systems," *Ann. Biomed. Eng.*, vol. 16, no. 1, pp. 143–157, 1988.
- [41] S. Srinivasan, F. Kallel, and J. Ophir, "Estimating the elastographic signal-to-noise ratio using correlation coefficients," *Ultrasound Med. Biol.*, vol. 28, pp. 359–368, Mar. 2002.
- [42] J.-L. Gennisson, T. Deffieux, R. Sinkus, P. Annic, M. Pernot, F. Cudeiro, G. Montaldo, M. Tanter, M. Fink, and J. Bercoff, "A 3-D elastography system based on the concept of ultrasound-computed tomography for in vivo breast examination," in *Proc. IEEE Ultrason. Symp.*, 2006, pp. 1037–1040.



Hani Eskandari (S'04) was born in Tehran, Iran in 1980. He received his B.Sc. degree in electrical engineering in 2001 and his M.Sc. degree in biomedical engineering in 2003 from Sharif University of Technology, Tehran, Iran. He is currently a Ph.D. student in electrical and computer engineering in the University of British Columbia, Vancouver, Canada.

Hani's research interests are in the fields of parameter estimation, inverse problems, Mechatronics and biomedical signal processing. His particular interests are currently elastography, finite elements modeling and mechanical parameter identification of soft tissues.



Septimiu (Tim) E. Salcudean (S'78–M'79–SM'03–F'05) received the B.Eng. and M.Eng. degrees from McGill University and the Ph.D. degree from U.C. Berkeley, all in electrical engineering.

From 1986 to 1989, he was a Research Staff Member in the robotics group at the IBM T.J. Watson Research Center. He then joined the Department of Electrical and Computer Engineering at the University of British Columbia, Vancouver, Canada, where he is now a Professor and holds a Canada Research Chair. He spent one year at ONERA-CERT (aerospace-controls laboratory) in Toulouse, France, in 1996–1997, where he held a Killam Research Fel-

lowship, and six months, during 2005, in the medical robotics group (GMCAO) at CNRS in Grenoble, France.

Dr. Salcudean is interested in medical robotics and ultrasound image guidance, elastography, haptic interfaces and virtual environments. Prof. Salcudean has been a co-organizer of several symposia on haptic interfaces and a Technical and Senior Editor of the *IEEE Transactions on Robotics and Automation*. He is a Fellow of the Canadian Academy of Engineering.



Robert Rohling (M'00) received the B.A.Sc. degree in engineering physics from the University of British Columbia (UBC), the M.Eng. degree in biomedical engineering from McGill University, and the Ph.D. degree in information engineering from the University of Cambridge. He worked as the project manager of 3D medical imaging at ALI Technologies from 1999–2000, before joining the University of British Columbia where he is now Associate Professor. He is a working member of DICOM on multidimensional interchange. He

is a member of Precarn Inc. as part of a Network of Centres of Excellence. He is also the coordinator of the Biomedical Engineering Option and co-coordinator of the Mechatronics program at UBC. In 2002, he was awarded a New Opportunities Fund Award from the Canada Foundation for Innovation to establish a research laboratory called the Ultrasound Innovation Laboratory. His current research areas include adaptive ultrasound, 3D ultrasound, elastography and image-guided surgery.